Robust Noise Filtering in Wideband Frequency-Invariant Beamforming with Uniform Circular Arrays

Camillo Gentile
National Institute of Standards and Technology
Emerging and Mobile Network Technologies Group
Gaithersburg, Maryland, USA
camillo.gentile@nist.gov

***Abstract*— Accurate signal measurement in the spatial-temporal domain is critical, amongst other applications, to the commercial success of UWB-MIMO communication systems and UWB standalone location systems. Antenna arrays can measure the spatial dimension of a signal through beamforming; to this end we chose to implement the uniform circular array in our spatial-temporal channel sounder due to its constant beam pattern around the azimuth angle. In wideband systems such as ours, it is important that the beam pattern also be constant across the band of operation to enable linear methods for multipath extraction or sidelobe suppression. Frequency-invariant beamforming can achieve this but at the expense of greater noise. Most literature treating the practical implementation of frequency-invariant beamforming concentrates on mutual coupling and physical-array imperfection. Rather in this paper we propose a novel filtering technique specific to the characteristic noise in frequency-invariant beamforming. It employs the eigendecomposition followed by least-squares minimization and proves robust even at low signal-to-noise ratios as substantiated through simulations as well as measurements using our sounder.**

***Index Terms*— Eigendecomposition, UWB-MIMO, UWB location, kurtosis**

I. Introduction

Ultra-Wideband (UWB) technology is characterized by a bandwidth greater than 500 MHz or exceeding 20% of the center frequency of radiation [1]. Despite the potential for high-speed communications, the FCC mask of -41.3 dBm/MHz EIRP in the spectrum 3.1–10.6 GHz translates to a maximum transmission power of -2.6 dBm. This limits applications to moderate data rates or short range. Multiple-Input Multiple-Output (MIMO) communication systems exploit spatial diversity by combining multipath arrivals from different directions to drastically improve link robustness or range [2]. UWB lends to MIMO by enabling multipath resolution through its fine time pulses. The fact that most UWB applications are geared towards indoor environments rich in scattering provides an ideal reception scenario for MIMO implementation; in addition, the GHz center frequency relaxes the mutual-coupling requirements on the spacing between antenna array elements. For these reasons UWB and MIMO fit hand-in-hand, making the best possible use of radiated power to promote the commercial success of Ultra-Wideband communication systems.

Ultra-Wideband technology is also the most promising for precision location systems: its fine time resolution and the presence of lower frequencies in the signal to penetrate walls enable UWB ranging systems to extract the first multipath arrival corresponding to the range between a transmitter and receiver, even when attenuated in strength compared to later arrivals. Bearing systems alone lack any notion of time and in general select the strongest arrival which is rarely the first one in non line-of-sight conditions. Complementing UWB ranging systems with bearing capabilities allows indexing the arrivals as a function of both time and angle in order to isolate the first, providing precision range and angle. If both the range and angle of a mobile station are known with respect to a base station, then the base station alone can extract the location of the mobile with no need for additional infrastructure. This is particularly useful in emergency operations such as fire rescue.

Critical to effectiveness of the aforementioned systems is accurate signal measurement in the spatial-temporal domain. Antenna arrays can be used to resolve the angles of multipath arrivals through beamforming. In our previous work on spatial-temporal channel sounding in the 2-8 GHz spectrum [3] and on UWB standalone location systems [4], we chose to implement the uniform circular array (UCA) over the uniform linear array (ULA) due to the following main advantages [5], [6], [7], [8], [9]: 1) the azimuth of the UCA covers 360° in contrast to 180°; 2) the beam pattern of the UCA is constant around the azimuth angle while that of the ULA broadens as the beam is steered from the boresight; 3) the UCA offers greater interference rejection for an equivalent number of elements. Despite these advantages, conventional beamforming in uniform circular arrays generates frequency-dependent beam patterns; when synthesized in wideband systems, the resultant sidelobes [10] are relatively large with respect to the ULA and due to their complexity linear methods [11], [12], [13], [14], [15] cannot be used for multipath extraction or sidelobe suppression. Conversely, *frequency-invariant beamforming* (FIB) achieves a constant beam pattern over any band of operation by transforming the physical-array response into a virtual-array response. The transformation however is susceptible to even minute traces of noise, potentially amplifying the noise of certain *corrupted* components in the response above the signal level.

Most literature treating the practical implementation of frequency-invariant beamforming concentrates on mutual coupling and physical-array imperfection [15], [16], [17]. Rather in this paper we propose a novel filtering technique specific to the characteristic noise in frequency-invariant beamforming. The paper reads as follows: Section II describes the spatial-temporal channel response together with the diversity methods

This full text paper was peer reviewed at the direction of IEEE Communications Society subject matter experts for publication in the IEEE "GLOBECOM" 2009 proceedings.

we employed to record a response using our system. Section III then introduces frequency-invariant beamforming followed by its noise analysis in the subsequent section. We propose our novel filtering technique in Section V which exploits the eigendecomposition followed by least-squares minimization. The numerical results in section VI substantiate the robustness of the technique at low signal-to-noise ratios for varying simulated responses, complemented by results from responses measured using our spatial-temporal channel sounder. The last section summarizes our conclusions.

II. The Spatial-Temporal Channel Response

The traditional model for the wideband propagation channel is a *temporal response* composed from K multipath arrivals indexed through k [18]

$$h(t) = \sum_{k=0}^{K-1} \alpha_k \delta(t - \tau_k), \tag{1}$$

where τ_k denotes the delay of the arrival in propagating between the transmitter and the receiver and α_k denotes the complex-valued amplitude which accounts for both attenuation and phase change due to reflection, diffraction, and other specular effects imposed by objects on its path.

The temporal response has a *frequency response*

$$H(\omega_l) = \sum_{k=0}^{K-1} \alpha_k e^{-j\omega_l \tau_k}, \tag{2}$$

suggesting that the channel can be characterized through *frequency diversity*: $H(\omega_l) = \frac{Y(\omega_l)}{X(\omega_l)}$ is computed by transmitting L tones $X(\omega_l)$ across the channel at uniform intervals of ω_l, $l = 0 \ldots L-1$ and then measuring $Y(\omega_l)$ at the receiver. In our previous work, we chose to implement a stepped-frequency system over transmitting a fixed pulse and recording the temporal response directly. The former offered the advantage of first sweeping the 2-8 GHz band of interest and then selecting subbands and pulse shapes a posteriori in varying the parameters of the system. The discrete frequency spectrum $H(\omega_l)$ transforms to the temporal domain as a periodic signal with revolution $\frac{2\pi}{\Delta\omega}$ [19], so $\Delta\omega$ must be chosen small enough to accommodate the maximum multipath spread expected in an environment to allow the arrivals to subside within one period and avoid time aliasing.

Replacing the single antenna at the receiver with a uniform circular array introduces *spatial diversity* into the system. This enabled us to measure both the spatial and temporal properties of the channel, in particular to index the arrivals as a function of azimuth angle ϕ_k as well. Fig. 1 shows a diagram of a single antenna transmitter and a uniform circular array receiver. The P elements of the UCA are arranged uniformly around its perimeter of radius r, each at angle $\theta_p = \frac{2\pi p}{P}$, $p = 0 \ldots P-1$. Let $H(\omega_l)$ be the frequency response between the transmitter and the center of the receiver. Arrival k approaching from angle ϕ_k hits element p with an additional delay $\tau_{k_p} = -\frac{r}{c}\cos(\phi_k - \theta_p)$ with respect to the delay τ_k at the center [20], so the *element-frequency response*

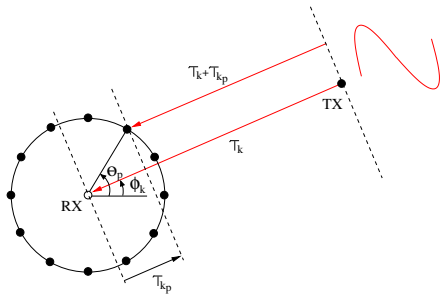

Fig. 1. The uniform circular array antenna.

is a phase-shifted version of $H(\omega_l)$, or

$$\begin{aligned} H_p(\omega_l) &= \sum_{k=0}^{K-1} \alpha_k e^{-j\omega_l(\tau_{k_p}+\tau_k)} \\ &= \sum_{k=0}^{K-1} \alpha_k e^{j\omega_l \frac{r}{c}\cos(\phi_k-\theta_p)} e^{-j\omega_l\tau_k} \end{aligned} \tag{3}$$

In conventional beamforming, the *spatial-frequency response* $H(\omega_l, \theta)$ is generated by shifting the phase of each element into alignment with respect to the center [20]:

$$H(\omega_l, \theta) = \frac{1}{P}\sum_{p=0}^{P-1} H_p(\omega_l) e^{-j\omega_l \frac{r}{c}\cos(\theta-\theta_p)} \tag{4}$$

From it, the *spatial-temporal response* $h(t, \theta)$ can be recovered by synthesizing the L tones through the Inverse Discrete Fourier Transform (IDFT):

$$h(t, \theta) = \frac{1}{L}\sum_{l=0}^{L-1} H(\omega_l, \theta) e^{j\omega_l t} \tag{5}$$

The ω_l-θ dependence inherent to the phase of (4) causes the beam pattern of $H(\omega_l, \theta)$ to vary according to the frequency of operation. This in turn generates intractable sidelobes in $h(t, \theta)$ with zero-crossings which vary jointly in the t and θ domains as illustrated in Fig. 2(a), precluding super-resolution algorithms for multipath extraction and windowing for sidelobe suppression.

III. Frequency-Invariant Beamforming

In narrowband systems, numerous filtering techniques [20], [21], [22] exist to shape the beam pattern of the array frequency response by applying complex weights to the terms in (4). In wideband systems such as ours, these techniques could be employed, but would require designing separate filters for each frequency; even so, it would be difficult to achieve the same beam pattern across the whole band with a finite number of elements. Frequency-invariant beamforming can achieve a constant beam pattern over a wide frequency band of operation. This class of filters has existed over a decade for uniform linear arrays, but have recently been adapted to uniform circular arrays. They have found application primarily in directional filtering and angle-of-flight estimation [23], [24],

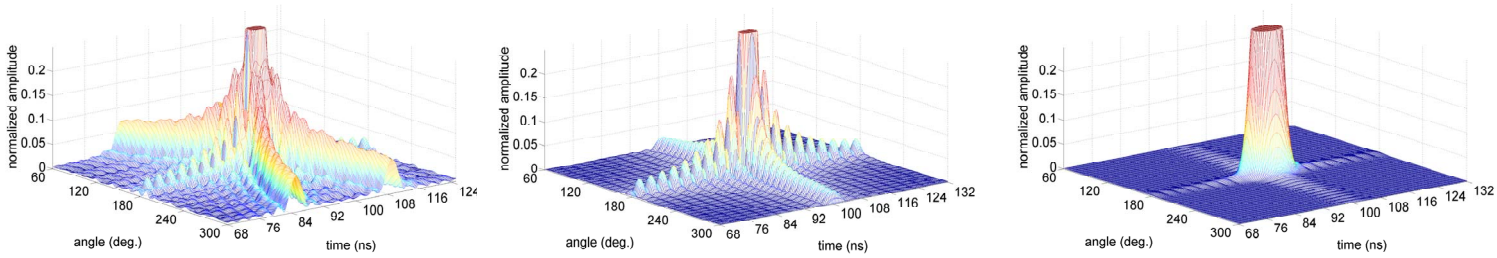

(a) Unit conventional $h(t,\theta)$ (b) Unit frequency-invariant $\hat{h}(t,\theta)$ (c) Unit frequency-invariant $\hat{h}(t,\theta)$ with suppressed sidelobes

Fig. 2. Comparison of the unit spatial-temporal response generated from conventional and frequency-invariant beamforming

but to our knowledge we are the first to employ them in joint time and angle-of-flight estimation.

The development of the frequency-invariant beamforming with the uniform circular array hinges on the expansion

$$e^{j\beta\cos\gamma} = \sum_{n=-\infty}^{\infty} j^n J_n(\beta) e^{jn\gamma}, \tag{6}$$

where $J_n(\beta)$ is Bessel function. The expansion enables separating the phase of the element-frequency response in (3) into frequency-dependent and independent components:

$$H_p(\omega_l) = \sum_{k=0}^{K-1} \alpha_k \left[\sum_{n=-\infty}^{\infty} j^n J_n(\omega_l \frac{r}{c}) e^{jn(\phi_k - \theta_p)} \right] e^{-j\omega_l \tau_k} \tag{7}$$

The angle ϕ_k can then be isolated in the above expression by introducing basis functions $e^{jm\theta_p}$ known as *phase modes* (or modes) as in the sequel:

$$\begin{aligned}
(a)\ \hat{H}_m(\omega_l) &= \frac{1}{P} \sum_{p=0}^{P-1} H_p(\omega_l) \cdot G_m(\omega_l) e^{jm\theta_p} \\
(b) \qquad &\approx \sum_{k=0}^{K-1} \alpha_k \Gamma \cdot e^{-j\omega_l \tau_k} \\
(c) \qquad &\approx \sum_{k=0}^{K-1} \alpha_k e^{jm\phi_k} \cdot e^{-j\omega_l \tau_k}
\end{aligned} \tag{8}$$

$$\begin{aligned}
(d)\ \Gamma &= \sum_{n=-\infty}^{\infty} j^n J_n(\omega_l \frac{r}{c}) e^{jn\phi_k} \cdot G_m(\omega_l) \left[\frac{1}{P} \sum_{p=0}^{P-1} e^{-j(n-m)\frac{2\pi p}{P}} \right] \\
(e) \quad &\approx j^m J_m(\omega_l \frac{r}{c}) e^{jm\phi_k} \cdot G_m(\omega_l) \\
(f) \quad &\approx e^{jm\phi_k}
\end{aligned}$$

Transform the element-frequency response into the *mode-frequency response* $\hat{H}_m(\omega_l)$ in (8a) by multiplying each $H_p(\omega_l)$ by the m^{th}-mode weighted by $G_m(\omega_l)$. Substitute (7) into the expression and rearrange as in (8b) using the placeholder Γ defined in (8d) to avoid clutter. Note that the bracketed term in (8d) is equal to 1 for $n = m + P \cdot z,\ z \in \mathcal{Z}$ and 0 otherwise, limiting the values of n in the sum. From [17], the Bessel function has the following property

$$\left| J_{|n|}(\omega_l \frac{r}{c}) \right| \leq \left(\frac{\omega_l \frac{r}{c} e}{2|n|} \right)^{|n|}, \tag{9}$$

so there exists a number of elements P sufficiently large such that $\left| J_{|n|}(\omega_l \frac{r}{c}) \right| \approx 0$ for $|n| > \frac{P-1}{2}$; but the latter condition is always met except for $z = 0$, so the Bessel function in turn is approximately zero except for $n = m$, limiting further the values of n and simplifying (8d) to (8e). By selecting $G_m(\omega_l) = 1/j^m J_m(\omega_l \frac{r}{c})$, Γ simplifies further to (8f).

The Vandermonde structure [15] of $\hat{H}_m(\omega_l)$ in (8c) in terms of m makes it amenable to the IDFT as a means to generate the FIB spatial-frequency response $\hat{H}(\omega_l, \theta)$ by transforming it from the mode domain to the spatial domain:

$$\hat{H}(\omega_l, \theta) = \frac{1}{M} \sum_{m=-\frac{P-1}{2}}^{\frac{P-1}{2}} \hat{H}_m(\omega_l) e^{jm\theta} \tag{10}$$

Note in contrast to the conventional $H(\omega_l, \theta)$ that the phase is now frequency independent. As explained previously, $|J_{|m|}(\omega_l \frac{r}{c})| \approx 0$ (and in turn $G_m(\omega_l)$ in (8e) approaches ∞) for $|m| > \frac{P-1}{2}$), so we include only $M = P$ modes in the Fourier sum above to avoid numerical instability. In our system the upper frequency f = 8 GHz in the band of operation imposes a minimum number of P = 97 elements to meet the approximation for the radius r = 24 cm of our UCA.

Finally the FIB spatial-temporal response $\hat{h}(t, \theta)$ can be recovered by replacing $H(\omega_l, \theta)$ in (5) instead with $\hat{H}(\omega_l, \theta)$. Fig. 2(b) illustrates the unit response for $\hat{h}(t, \theta)$ and Fig. 2(c) illustrates the unit response processed using a two-dimensional Kaiser window.

IV. Noise Analysis in FIB

While frequency-invariant beamforming provides a powerful means for multipath extraction or sidelobe suppression in uniform circular arrays, it is susceptible to even minute traces of noise. Here we analyze the FIB characteristic noise and outline the eigendecomposition for noise filtering in prelude to the subsequent section. Let each component of the element-frequency response be perturbed by i.i.d. additive white Gaussian noise (AWGN) $W_p(\omega_l) \sim \mathcal{N}(0, \sigma)$:

$$X_p(\omega_l) = H_p(\omega_l) + W_p(\omega_l) \tag{11}$$

Replacing $H_p(\omega_l)$ in (8a) with the *noisy* element-frequency response above and working through the development yields

the noisy mode-frequency response

$$\begin{aligned}\hat{X}_m(\omega_l) &= \hat{H}_m(\omega_l) + \hat{W}_m(\omega_l), \qquad (12)\\ \hat{W}_m(\omega_l) &= \frac{1}{j^m J_m(\omega_l \frac{r}{c})} \cdot \frac{1}{P} \sum_{p=0}^{P-1} W_p(\omega_l) e^{jm\theta_p}.\end{aligned}$$

It is well known that a linear sum of zero-mean Gaussian-distributed variables such as $\hat{W}_m(\omega_l)$ is also zero-mean Gaussian distributed [25]. It follows that $\hat{W}_m(\omega_l) \sim \mathcal{N}(0, \sqrt{\mathcal{E}[\hat{W}_m(\omega_l)\hat{W}_m^*(\omega_l)]}\,)$ since the variance is then equal to the second moment which is computed as

$$\begin{aligned}\mathcal{E}[\hat{W}_m(\omega_l)\hat{W}_m^*(\omega_l)] = \mathcal{E}\Bigg[&\frac{1}{j^m J_m(\omega_l \frac{r}{c})} \frac{1}{P} \sum_{p=0}^{P-1} W_p(\omega_l) e^{jm\theta_p} \cdot \\ &\frac{1}{j^{-m} J_m(\omega_l \frac{r}{c})} \frac{1}{P} \sum_{q=0}^{P-1} W_q^*(\omega_l) e^{-jm\theta_q} \Bigg] = \\ &\frac{1}{\left[P J_m(\omega_l \frac{r}{c})\right]^2} \sum_{p=0}^{P-1} \left\{ \sum_{q=0}^{P-1} \mathcal{E}[W_p(\omega_l) W_q^*(\omega_l)] e^{jm(\theta_p - \theta_q)} \right\} = \\ &\frac{\sigma^2}{P\left[J_m(\omega_l \frac{r}{c})\right]^2}, \qquad (13)\end{aligned}$$

where $\mathcal{E}$ is the expectation operator. Note that the Bessel function $J_m(\omega_l \frac{r}{c})$ is real-valued and that the braced expression reduces to σ^2 since the element noise is AWGN, implying $\mathcal{E}[W_p(\omega_l)W_p^*(\omega_l)] = \sigma^2$ and $\mathcal{E}[W_p(\omega_l)W_q^*(\omega_l)] = 0,\ q \neq p$.

A. The eigendecomposition

Consider vectorizing the $M \times L$ response matrix $\hat{X}_m(\omega_l), m = -\frac{P-1}{2} \ldots \frac{P-1}{2}, l = 0 \ldots L$ into an ML-dimensional vector $\hat{\mathbf{X}}$ through the VEC operator defined below:

$$\begin{aligned}\hat{\mathbf{X}} &= \text{VEC}\left\{ \hat{X}_{[-\frac{P-1}{2} \ldots \frac{P-1}{2}]}([\omega_0 \cdots \omega_{L-1}]) \right\} \qquad (14)\\ &:= [\hat{X}_{-\frac{P-1}{2}}(\omega_0)\ \hat{X}_{-\frac{P-1}{2}}(\omega_1) \cdots \hat{X}_{-\frac{P-1}{2}}(\omega_{L-1}) \vdots \\ &\quad \hat{X}_{-\frac{P-1}{2}+1}(\omega_0)\ \hat{X}_{-\frac{P-1}{2}+1}(\omega_1) \cdots \hat{X}_{-\frac{P-1}{2}+1}(\omega_{L-1}) \vdots \cdots \vdots \\ &\quad \hat{X}_{\frac{P-1}{2}}(\omega_0)\ \hat{X}_{\frac{P-1}{2}}(\omega_1) \cdots \hat{X}_{\frac{P-1}{2}}(\omega_{L-1})]^T\end{aligned}$$

The response matrix can then be rewritten in vector form as

$$\hat{\mathbf{X}} = \hat{\mathbf{H}} + \hat{\mathbf{W}} = \mathbf{V}\mathbf{a} + \hat{\mathbf{W}}, \qquad (15)$$

where

$$\begin{aligned}\hat{\mathbf{H}} &= \text{VEC}\left\{ \hat{H}_{[-\frac{P-1}{2} \ldots \frac{P-1}{2}]}([\omega_0 \cdots \omega_{L-1}]) \right\},\\ \hat{\mathbf{W}} &= \text{VEC}\left\{ \hat{W}_{[-\frac{P-1}{2} \ldots \frac{P-1}{2}]}([\omega_0 \cdots \omega_{L-1}]) \right\},\\ \mathbf{v}_k &= \text{VEC}\left\{ e^{j[0 \cdots M-1]\phi_k} \cdot e^{-j\Delta\omega[0 \cdots L-1]\tau_k} \right\},\\ \mathbf{V} &= [\mathbf{v}_0\ \mathbf{v}_1 \cdots \mathbf{v}_{K-1}], \text{and}\\ \mathbf{a} &= [a_0\ a_1 \cdots a_{K-1}]^T,\ a_k = \alpha_k e^{j(-\frac{P-1}{2})\phi_k} \cdot e^{-j\omega_0\tau_k}.\end{aligned}$$

Following the development in [19], the eigendecomposition factorizes the autocorrelation matrix of $\hat{\mathbf{X}}$, denoted as $\mathbf{R}_{\hat{\mathbf{X}}}$, into ML eigenvalues and eigenvectors. It can then be separated into two terms known as the signal autocorrelation matrix and the noise covariance matrix respectively

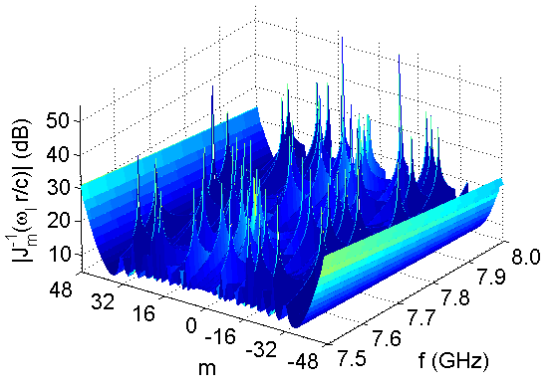

Fig. 3. The large variance of the Bessel amplitude in the mode and frequency components.

$$\mathbf{R}_{\hat{\mathbf{X}}} = E(\hat{\mathbf{X}}\hat{\mathbf{X}}^H) = \mathbf{V}\mathbf{R}_{\mathbf{a}}\mathbf{V}^H + \frac{\sigma^2}{P}\mathbf{D}^{-2}(\mathbf{J}), \qquad (16)$$

where $\mathbf{R}_{\mathbf{a}} = \mathcal{E}(\mathbf{a}\mathbf{a}^H)$, $\mathbf{J} = \text{VEC}\left\{ J_{[-\frac{P-1}{2} \ldots \frac{P-1}{2}]}([\omega_0 \cdots \omega_{L-1}]\frac{r}{c}) \right\}$, and $\mathbf{D}(\mathbf{J})$ is the square matrix with $\mathbf{J}$ on the diagonal. Since the column vectors of $\mathbf{V}$ adhere to the Vandermonde structure, the $ML \times K$ matrix maintains full column rank given that the arrival angles ϕ_k and delays τ_k are pairwise different (otherwise they could not be resolved). While the magnitude $|\alpha_k|$ of the complex amplitude $\alpha_k = |\alpha_k| e^{j\angle\alpha_k}$ is constant from one time sample to the next, the angle $\angle\alpha_k$ is well established as a uniform random variable $\mathcal{U}[0, 2\pi)$ [18], hence the $K \times K$ autocorrelation matrix $\mathbf{R}_{\mathbf{a}}$ is also full rank. Then for $ML > K$, $\text{rank}(\mathbf{V}\mathbf{R}_{\mathbf{a}}\mathbf{V}^H) = K$ and the eigenvectors corresponding to the K largest eigenvalues are called the signal eigenvectors while the remaining $ML-K$ are called the noise eigenvectors. Thus, the ML-dimensional space containing $\hat{\mathbf{X}}$ can be split into two orthogonal subspaces, known as the signal subspace and the noise subspace, spanned by the signal eigenvectors $\mathbf{q}_i, i = 0 \ldots K-1$ and the noise eigenvectors $\mathbf{q}_i, i = K \ldots ML-1$ respectively. The projection matrix of the noise subspace is then determined by

$$\mathbf{P} = \mathbf{Q}_{\hat{\mathbf{W}}}\mathbf{Q}_{\hat{\mathbf{W}}}^H, \qquad (17)$$

where $\mathbf{Q}_{\hat{\mathbf{W}}} = [\mathbf{q}_K\ \mathbf{q}_{K+1} \cdots \mathbf{q}_{ML-1}]$. Then the following relationship holds true

$$\mathbf{P}\hat{\mathbf{X}} = \hat{\mathbf{W}}. \qquad (18)$$

V. Robust Noise Filtering in FIB

The eigencomposition is useful in separating the noise $\hat{\mathbf{W}}$ from the noisy response $\hat{\mathbf{X}}$ through the noise projection matrix $\mathbf{P}$ as in (18). However it can be seen through (12) that the mode-frequency noise scales with the inverse of the Bessel amplitude $|J_m^{-1}(\omega_l \frac{r}{c})|$. Fig. 3 illustrates the matrix $|J_m^{-1}(\omega_l \frac{r}{c})|$ in dB for $m = -48 \ldots 48$ and $f = \frac{\omega}{2\pi} = 7.5 - 8$ GHz. Since the minimum value in the matrix is 6.92 dB, the magnitude of the mode-frequency noise is always greater than that of

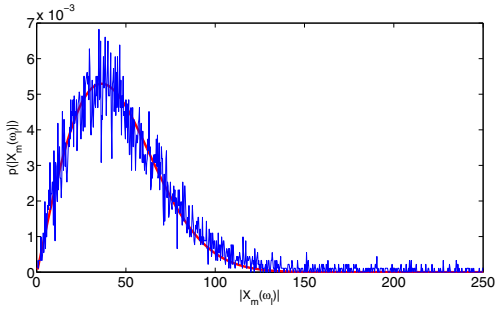

(a) Distribution of $|\hat{X}_m(\omega_l)|$

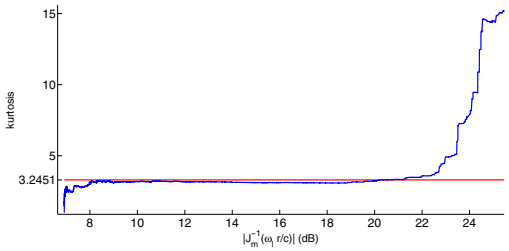

(b) Kurtosis of $\hat{\mathbf{X}}^U$

Fig. 4. Kurtosis is used to isolate the corrupted components in the noisy mode-frequency response

the the element-frequency noise; moreover, there exist many matrix components for which the Bessel amplitude lies several orders of magnitude above the minimum value, potentially magnifying the respective noise component $\hat{W}_m(\omega_l)$ above the level of the signal $\hat{H}_m(\omega_l)$ and in turn corrupting $\hat{X}_m(\omega_l)$. If $\hat{\mathbf{X}}$ contains *corrupted* components it cannot be used in its entirety to compute the covariance matrix; otherwise some noise eigenvalues may be larger than the signal eigenvalues, inhibiting clear separation between the two subspaces. In this section, we describe our novel filtering technique to recover the corrupted components from the *uncorrupted* components.

1) Isolate the corrupted components:
The first step in our technique is to partition $\hat{\mathbf{X}}$ into disjoint sets of corrupted $\hat{X}_m(\omega_l) \in \hat{\mathbf{X}}^C : |J_m^{-1}(\omega_l \frac{r}{c})| > \zeta$ and uncorrupted $\hat{X}_m(\omega_l) \in \hat{\mathbf{X}}^U : |J_m^{-1}(\omega_l \frac{r}{c})| \leq \zeta$ components as determined by the threshold ζ. The uniform phase of the arrivals gives rise to a Rayleigh distribution for the amplitude of the response $\hat{H}_m(\omega_l)$ [26]. As an example, consider the amplitude distribution shown in blue in Fig. 4(a) of the noisy response $\hat{X}_m(\omega_l)$ measured using our system. The amplitude fluctuates around a robust fit shown in red of the Rayleigh distribution to the data. At smaller values of $\hat{X}_m(\omega_l)$, the noise in the components is small and so the data fits well, but at values beyond 70 the data deviates and lies more and more above the fit, indicating large noise in the components. The *kurtosis* characterizes the sharpness of a distribution and is defined for $|\hat{\mathbf{X}}^U|$ as

$$\begin{aligned} \mathcal{K}(|\hat{\mathbf{X}}^U|) &= \frac{\mu_4}{\mu_2^2}, \qquad (19) \\ \mu_n &= \frac{1}{\text{card}(\hat{\mathbf{X}}^U)} \sum_{\substack{\hat{X}_m(\omega_l):\\ \hat{X}_m(\omega_l) \in \hat{\mathbf{X}}^U}} (|\hat{X}_m(\omega_l)| - \mu_1)^n, \end{aligned}$$

where $\text{card}(\hat{\mathbf{X}}^U)$ denotes the number of components in $\hat{\mathbf{X}}^U$ and μ_n the n^{th} central moment. The kurtosis for the Rayleigh distribution is approximately 3.2451 [27]. Similar to its application in [28], as ζ increases from 0 more values are included in the distribution, boosting its sharpness (low kurtosis value); however beyond a certain value, the corrupt components flatten the peak more and more (high kurtosis value). Fig. 4(b) displays the kurtosis versus ζ. The kurtosis is equal to 3.2451 for ζ = 20.67 dB corresponding to 19.1% corrupted components in $\hat{\mathbf{X}}$.

2) Compute the noise projection matrix:
Rather than compute the noise projection matrix from $\mathbf{R}_{\hat{\mathbf{X}}}$, we segment the $M \times L$ response matrix $\hat{X}_m(\omega_l)$ into $\tilde{M} \times \tilde{L}$ *submatrices*. Each are subsequently vectorized into the $\tilde{M}\tilde{L}$-dimensional vector

$$\begin{aligned} \hat{\mathbf{X}}_{ml} = \text{VEC}\left\{\hat{X}_{[m\cdots m+\tilde{M}-1]}([\omega_l \cdots \omega_{l+\tilde{L}-1}])\right\}, \qquad (20) \\ 1 \leq \tilde{M} \leq M,\ -\tfrac{P-1}{2} \leq m \leq \tfrac{P-1}{2} - \tilde{M} + 1, \\ 1 \leq \tilde{L} \leq L,\ 0 \leq l \leq L - \tilde{L} + 1. \end{aligned}$$

Adjacent submatrices are shifted by one in either the mode or frequency dimension and so are overlapping for $\tilde{M} > 1$ or $\tilde{L} > 1$ respectively.

Now the *sample autocorrelation matrix* can be computed by incorporating in the sum only those N submatrices which contain no corrupted components:

$$\bar{\mathbf{R}}_{\hat{\mathbf{X}}} = \frac{1}{N} \sum_{\substack{\forall \hat{\mathbf{X}}_{ml}:\\ \hat{\mathbf{X}}_{ml} \cap \hat{\mathbf{X}}^C = \emptyset}} \hat{\mathbf{X}}_{ml} \hat{\mathbf{X}}_{ml}^H \qquad (21)$$

The mode-frequency Vandermonde structure of $\hat{\mathbf{X}}_{ml}$ makes it amenable to two-dimensional smoothing in computing $\bar{\mathbf{R}}_{\hat{\mathbf{X}}}$ [29], [30]. The well-known spatial smoothing technique [31] serves to decorrelate the arrivals and in the process augments the rank of the matrix to $\min(N, \tilde{M}\tilde{L})$. Note that the sample autocorrelation matrix must have full rank to enable factorization into K signal eigenvectors and $\tilde{M}\tilde{L} - K$ noise eigenvectors, implying $N \geq \tilde{M}\tilde{L}$. We employ the Minimum Description Length (MDL) criteria described in [32] to furnish an estimated number of arrivals $\tilde{K}$. Since it cannot be estimated prior to computing $\bar{\mathbf{R}}_{\hat{\mathbf{X}}}$, the dimension of the submatrix should be chosen as large as possible to avoid $\tilde{M}\tilde{L} < \tilde{K}$ for which the technique obviously cannot be applied. Since the submatrix intrinsically has a reduced number of modes and a reduced bandwidth compared to the whole matrix, it may not have sufficient resolution to separate all the arrivals when $\tilde{M}\tilde{L} < K$. As a result they appear combined as $\tilde{K} \ll K$ in the sub-dimensional space such that $\tilde{M}\tilde{L} > \tilde{K}$. This is the key realization in our technique which is substantiated in the results section through experiments with measured responses.

Then the $\tilde{M} \times \tilde{L}$ dimension is set by maximizing $\tilde{M}\tilde{L}$ such that there exist at least $N \geq \tilde{M}\tilde{L}$ submatrices in the whole $M \times L$ matrix which contain no corrupted components. The condition can be relaxed to $N \geq \frac{1}{2}\tilde{M}\tilde{L}$ by using instead the *forward-backward autocorrelation matrix* [32]

$$\bar{\mathbf{R}}_{\hat{\mathbf{X}}}^{FB} = \frac{1}{2}(\bar{\mathbf{R}}_{\hat{\mathbf{X}}} + \mathbf{E}\bar{\mathbf{R}}_{\hat{\mathbf{X}}}^{*}\mathbf{E}) \tag{22}$$

which has twice the rank of $\bar{\mathbf{R}}_{\hat{\mathbf{X}}}$, where $\mathbf{E}$ is the $\tilde{M}\tilde{L} \times \tilde{M}\tilde{L}$ exchange matrix whose components are zeros except for ones on the antidiagonal.

Now we can invoke the noise projection matrix $\mathbf{P}_{ml}$ as in (18) to separate the noise $\hat{\mathbf{W}}_{ml}$ from the noisy response $\hat{\mathbf{X}}_{ml}$ through the analogous relationship

$$\mathbf{P}_{ml}\hat{\mathbf{X}}_{ml} = \hat{\mathbf{W}}_{ml}, \tag{23}$$

where $\hat{\mathbf{W}}_{ml} = \text{VEC}\left\{\hat{W}_{[m\cdots m+\tilde{M}-1]}([\omega_l \cdots \omega_{l+\tilde{L}-1}])\right\}$. $\mathbf{P}_{ml}$ is computed as in (17) from the noise eigenvalues given from the eigendecomposition of $\bar{\mathbf{R}}_{\hat{\mathbf{X}}}$, however note from (21) that the sample noise covariance matrix is $\frac{\sigma^2}{P}\mathbf{D}^{-2}(\bar{\mathbf{J}})$ where

$$\bar{\mathbf{J}} = \frac{1}{N}\sum_{\substack{\forall \hat{\mathbf{X}}_{ml}: \\ \hat{\mathbf{X}}_{ml} \cap \hat{\mathbf{X}}^C = \emptyset}} \mathbf{J}_{ml} \tag{24}$$

and $\mathbf{J}_{ml} = \text{VEC}\left\{J_{[m\cdots m+\tilde{M}-1]}([\omega_l \cdots \omega_{l+\tilde{L}-1}]\frac{r}{c})\right\}$. So the noise eigenvectors must be altered according to the procedure in [33] such that resultant sample noise covariance matrix matches the noise covariance matrix $\frac{\sigma^2}{P}\mathbf{D}^{-2}(\mathbf{J}_{ml})$ of $\hat{\mathbf{X}}_{ml}$. This noise *coloring* procedure is similar to noise whitening which is a standard pre-processing step in super-resolution algorithms [15], [19].

3) Recover the corrupted components:

In the last step of our technique, we designate the corrupted components $\hat{\mathbf{X}}_{ml}^{C}$ in a submatrix as *unknown* and recover them by minimizing the norm of the weighted noise defined as

$$||\mathbf{D}(\mathbf{J}_{ml})\hat{\mathbf{W}}_{ml}||_2 = \hat{\mathbf{W}}_{ml}^{H}\mathbf{D}^2(\mathbf{J}_{ml})\hat{\mathbf{W}}_{ml}. \tag{25}$$

The covariance matrix $\mathbf{D}^2(\mathbf{J}_{ml})$ of the weighted noise is now proportional to the inverse of the noise covariance matrix $\frac{\sigma^2}{P}\mathbf{D}^{-2}(\mathbf{J}_{ml})$, so the weight effectively whitens the noise by leveraging all components equally during minimization. If we reorder $\hat{\mathbf{X}}_{ml} = [\hat{\mathbf{X}}_{ml}^{C} \vdots \hat{\mathbf{X}}_{ml}^{U}]^T$ according to the corrupted (unknown) and uncorrupted (known) components and substitute (23) into (25), then the norm can be rewritten as

$$\|\mathbf{D}(\mathbf{J}_{ml})\mathbf{P}_{ml}\hat{\mathbf{X}}_{ml}||_2 = ||\mathbf{D}(\mathbf{J}_{ml})\mathbf{P}_{ml}^{C}\hat{\mathbf{X}}_{ml}^{C} - \mathbf{D}(\mathbf{J}_{ml})\mathbf{P}_{ml}^{U}\hat{\mathbf{X}}_{ml}^{U}||_2 \tag{26}$$

for the columns of $\mathbf{P}_{ml} = [\mathbf{P}_{ml}^{C} \vdots \mathbf{P}_{ml}^{U}]$ and the components of $\mathbf{J}_{ml} = [\mathbf{J}_{ml}^{C} \vdots \mathbf{J}_{ml}^{U}]$ reordered according to the same criterion. In this form, it can be readily seen that minimizing the norm simply reduces to solving a least-squares problem for $\hat{\mathbf{X}}_{ml}^{C}$.

Since the submatrices overlap and in turn share common unknowns, a tighter and moreover unique solution is found for the whole $\hat{\mathbf{X}}^C$ by minimizing the norm aggregately over all submatrices which contain corrupted components, stated formally as:

$$\min \sum_{\substack{\forall \hat{\mathbf{X}}_{ml}: \\ \hat{\mathbf{X}}_{ml} \cap \hat{\mathbf{X}}^C \neq \emptyset}} \|\mathbf{D}(\mathbf{J}_{ml})\mathbf{P}_{ml}\hat{\mathbf{X}}_{ml}\|_2 \tag{27}$$

Each submatrix contributes rank($\mathbf{D}(\mathbf{J}_{ml})\mathbf{P}_{ml}$) = rank($\mathbf{P}_{ml}$)[1] independent equations to the linear system. As explained in IV-A, rank($\mathbf{P}_{ml}$) is equal to the estimated number of noise eigenvalues $\tilde{M}\tilde{L} - \tilde{K}$.

VI. Results

This section substantiates the effectiveness of our noise filtering technique as applied to both measured and simulated responses. The former validates its application to real systems such as the spatial-temporal channel sounder we assembled in previous work [3], [4]. The system measures the response in the 2–8 GHz band using a vector network analyzer coupled to a virtual uniform circular array. The details of the system are included in the citations. Due to the computational intensity of our technique, in this paper we focus on the smaller 7.5–8 GHz subband. The frequency interval was set to Δf = 5 MHz for a total of L = 101 tones while M was set equal to the number of elements P = 97. Fig. 5(a) displays the spatial-temporal response generated from the original mode-frequency response $\hat{\mathbf{X}}$-$Orig$ measured in a corridor. In applying our technique, the number of corrupted components was determined from the kurtosis as 1870 out of 9797 total components, resulting in an 13 × 14 submatrix. The number of arrivals was estimated as $\tilde{K}$ = 76. Fig. 5(b) displays the spatial-temporal response generated from the filtered mode-frequency response $\hat{\mathbf{X}}$-$Filt$. Notice that much of the noise is filtered with the dominant arrivals approaching in angular clusters from opposite directions 180° and 360°, as expected in a corridor environment. Both responses were processed using a two-dimensional Kaiser window for sidelobe suppression.

Now we present the numerical results from simulated responses for which ground-truth data is available. We used the stochastic spatial-temporal channel propagation model described in [3] complete with 19 parameters to generate the element-frequency response vectorized as $\mathbf{H}$. AWGN $\mathbf{W}$ was scaled and then added to the response to achieve the three different levels for the signal-to-noise ratio SNR($\mathbf{X}$) of the noisy response $\mathbf{X} = \mathbf{H} + \mathbf{W}$ in Table I. The latter was subsequently transformed to the mode-frequency response $\hat{\mathbf{X}}$-$Orig$ and filtered as $\hat{\mathbf{X}}$-$Filt$ using our technique. The table lists the signal-to-noise ratio of the original corrupted components SNR($\hat{\mathbf{X}}^C$-$Orig$) and that of filtered corrupted components SNR($\hat{\mathbf{X}}^C$-$Filt$) for varying number of multipath arrivals K; it also provides the signal-to-noise ratio of the uncorrupted components SNR($\hat{\mathbf{X}}^U$) as a baseline. Each entry in the table was averaged over 10 trials. We see through SNR($\hat{\mathbf{X}}^U$) and SNR($\hat{\mathbf{X}}^C$-$Orig$) that the noise level of the mode-frequency response is higher than that of the element-frequency response, as expected since $|J_m^{-1}(\omega\frac{r}{c})| > 0$ dB.

[1] $\mathbf{D}(\mathbf{J}_{ml})$ is full rank assuming all values in $\mathbf{J}_{ml}$ are different.

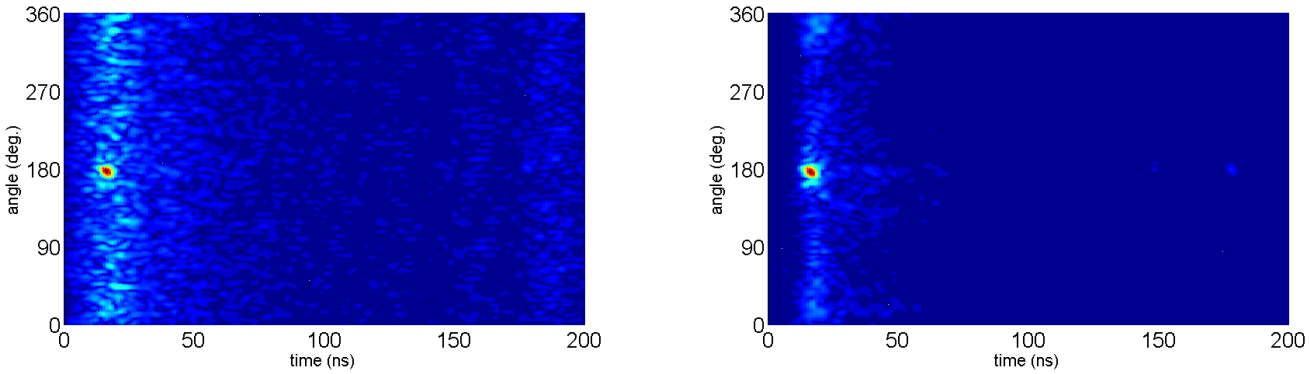

(a) Original $\hat{h}(t,\theta)$ (b) Filtered $\hat{h}(t,\theta)$

Fig. 5. Comparison of the spatial-temporal response generated from original and filtered measured responses

TABLE I

COMPARISON OF ORIGINAL AND FILTERED SIMULATED RESPONSES

SNR($\mathbf{X}$)	K		
	100	300	500
30	25.54	25.75	25.71
	-1.50	-2.34	-3.72
	28.17	26.50	25.73
20	17.30	17.55	17.49
	-3.34	-4.77	-5.12
	19.52	11.28	8.81
10	8.41	8.32	8.67
	-11.01	-16.49	-17.16
	7.63	6.85	5.32

LEGEND
SNR($\hat{\mathbf{X}}^U$)
SNR($\hat{\mathbf{X}}^C$-$Orig$)
SNR($\hat{\mathbf{X}}^C$-$Filt$)

Our technique is able to restore the corrupted components by several orders of magnitude in all test conditions, and note in particular that SNR($\hat{\mathbf{X}}^C$-$Filt$) $>$ SNR($\hat{\mathbf{X}}^U$) for all K and SNR($\mathbf{X}$) = 30 and for K = 100 and SNR($\mathbf{X}$) = 20. The technique works better for smaller K since rank($\mathbf{P}_{ml}$) = $ML - K$ is larger, providing a tighter solution to the linear system. The average percentage of corrupted components was 16.4% for SNR($\mathbf{X}$) = 30, 21.5% for SNR($\mathbf{X}$) = 20, and 26.0% for SNR($\mathbf{X}$) = 10.

In order to demonstrate the applicability of our technique even for the case $\tilde{M}\tilde{L} < K$ discussed in Subsection V-2, we consider a simulated response for K = 500 and SNR($\mathbf{X}$) = 20. In applying the technique, the dimension of the submatrix was determined as 12 $\times$ 20 while the number of arrivals was estimated as $\tilde{K}$ = 149. Fig. 6(a) shows a plot of the eigenvalues in the 240-dimensional space in which the asterisk marks $\tilde{K}$. Observe the clear separation between the signal and noise eigenvalues. As a post-processing step, we ran the eigendecomposition on the $\hat{\mathbf{X}}$-$Filt$ with no designated corrupted components. The dimension of the submatrix was determined as 58 $\times$ 58 and the number of arrivals was estimated as $\tilde{K}$ = 508 (very close to the ground-truth value), showing that all the arrivals can be resolved despite $\tilde{M}\tilde{L} < K$ in the sub-dimensional space. Fig. 6(b) shows a plot of the eigenvalues from $\hat{\mathbf{X}}$-$Filt$ in the 3364-dimensional space in blue. Again, a clear separation can be seen between the signal and noise eigenvalues. Note that the noise projection matrix can subsequently be used to separate the noise in $\hat{\mathbf{X}}$-$Filt$ also attributed to the unfiltered uncorrupted components. In fact, recall that in many test conditions in Table I $\hat{\mathbf{X}}^C$-$Filt$ has a higher signal-to-noise ratio than $\hat{\mathbf{X}}^U$. Finally as a proof of concept, we also ran the eigendecomposition on $\hat{\mathbf{X}}$-$Orig$ with no designated corrupted components, however the number of arrivals was estimated as $\tilde{K}$ = 763. This evidences that when incorporating the corrupted components, the eigendecomposition cannot discriminate between the two subspaces because the larger noise eigenvalues overlap with the signal eigenvalues and so are misclassified as signal eigenvalues. Fig. 6(b) shows a plot of the eigenvalues from $\hat{\mathbf{X}}$-$Orig$ in red. The jagged curve is uncharacteristic of signal eigenvalues.

While the aggregate norm in (25) can be minimized over all submatrices which contain corrupted components, in practice including them all may prohibitively increase the size of the linear system beyond available computational resources. In order for our filtering technique to work reliably, besides ensuring that all unknowns are including in the linear system, we have found through extensive experimentation that the number of independent equations should exceed the number of unknowns by a least a factor of 10 for SNR($\mathbf{X}$) = 30 and up to a factor of 30 for SNR($\mathbf{X}$) = 10. This provides enough samples for sufficient definition of the mode-frequency noise which is being minimized. Thereafter, the results improve but at diminishing returns.

VII. CONCLUSIONS

Our novel filtering technique has been shown as extremely effective through both simulation and measurement in recovering corrupted components in the noisy mode-frequency response. In some test conditions, it restored the signal by close to 30 dB and above the level of the uncorrupted components. As the signals because more complex in terms of the number of multipath arrivals, the performance degrades because the sub-dimensional space provides less definition of the mode-frequency noise vis-a-vis the number of independent equations in the linear system.

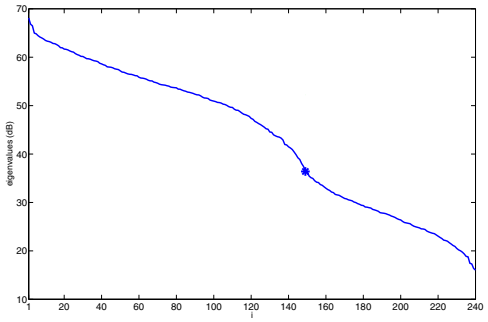

(a) Eigenvalues in sub-dimensional space

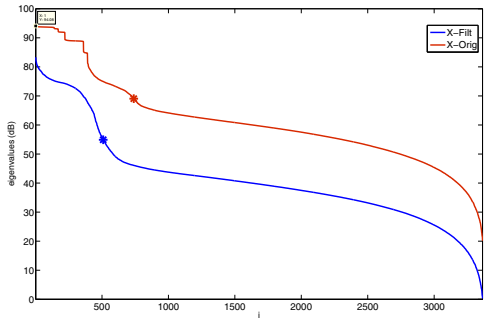

(b) Eigenvalues from $\hat{\mathbf{X}}$-$Orig$ and $\hat{\mathbf{X}}$-$Filt$

Fig. 6. Separation of signal and noise subspaces through the eigendecomposition

REFERENCES

[1] A.F. Molisch, "Ultrawideband Propagation Channels-Theory, Measurement, and Modeling," *IEEE Trans. on Vehicular Technology*, Vol. 54, No. 5, pp. 1528-1545, Sept. 2005.

[2] A. Sibille, "Time-Domain Diversity in Ultra-Wideband MIMO Communications," *EURASIP Journal on Applied Signal Processing*, vol. 3, pg. 316-327, 2005.

[3] C. Gentile, S. Martinez-Lopez, and A. Kik, "A Comprehensive Spatial-Temporal Propagation Model for the Ultra-Wideband Spectrum 2-8 GHz," *To appear in IEEE Trans. on Antennas and Propagation*, 2009.

[4] C. Gentile, A. Judson Braga, and Alfred Kik, "A Comprehensive Evalution of Joint Range and Angle Estimation in Indoor Ultrawideband Location Systems," *EURASIP Journal on Wireless Communications and Networking*, id. 248509, 2008.

[5] B. Allen and M. Ghavami, "Adaptive Array Systems: Fundamentals and Applications," *John Wiley and Sons*, pp. 156-160, 2005.

[6] Z. Huang and C.A. Balanis, "BER Performances of ULA and UCA in AWGN," *IEEE Antennas and Propagation Society Symp.*, pp. 4196=4199, June 2007.

[7] P. Ioannides and C.A. Balanis, "Uniform Circular and Rectangular Arrays for Adaptive Beamforming Applications," *IEEE Antennas and Propagation Letters*, vol. 4, pp. 351-354, 2005.

[8] L. Dong, C. Huang, J. Wang, and J. Zhou, "The Impact of Spatial Fading Correlation on SER Performance of Circular Array Versus Linear Array," *IEEE Conf. on Communications, Circuits, and Systems*, vol. 2, pp. 925-928, June 2006.

[9] J.-A. Tsai, R.M. Buehrer, and B.D. Woerner, "BER Performance of a Uniform Circular Array Versus a Uniform Linear Array in a Mobile Radio Environment," *IEEE Trans. in Wirless Communications*, vol. 3, no. 3, May 2004.

[10] F. Anderson, W. Christensen, L. Fullerton, and B. Kortegaard, "Ultra-wideband beamforming in sparse arrays," *IEE Proceedings-H on Microwaves, Antennas, and Propagation*, vol. 138, no. 4, pp. 342-346, Aug. 1991.

[11] C.M. Tan, P. Fletcher, M.A. Beach, A.R. Nix, M. Landmann, and R.S. Thoma, "On the Application of Circular Arrays in Direction Finding Part I: Investigation into the estimation algorithms," *First COST 273 Workshop*, May 2002.

[12] , Do-Hong, F. Demmel, and P. Russer, "A Method for Wideband Direction-of-Arrival Estimation Using Frequency-Domain Frequency-Invariant Beamformers," *IEEE Antennas and Propagation Society Symp.*, vol. 3, pp. 244-247, June 2003.

[13] D.B. Ward, Z. Ding, and R.A. Kennedy, "Broadband DOA Estimation Using Frequency Invariant Beamforming," *IEEE Trans. on Signal Processing*, vol. 46, no. 5, May 1998.

[14] Y. Yang, C. Wan, and C. Sun, "Broadband Beamspace DOA Estimation Algorithms," *IEEE OCEANS Proceedings*, vol. 3, pp. 1654-1660, Sept. 2003.

[15] M. Wax, "Direction Finding of Coherent Signals via Spatial Smoothing for Uniform Circular Arrays," *IEEE Trans. of Antennas and Propagation*, vol. 42, no. 5, pp. 613-620, May 1994.

[16] F. Belloni and V. Koivunen, "Beamspace Transform for UCA: Error Analysis and Bias Reduction," *IEEE Trans. on Signal Processing*, vol. 54, no. 8, pp, 3078-3089, Aug. 2006.

[17] S.C. Chan and H.H. Chen, "Uniform Concentric Circular Arrays with Frequency-Invariant Characteristics–Theory, Design, Adaptive Beamforming and DOA Estimation," *IEEE Trans. on Signal Processing*, vol. 55, no. 1, pp. 165-177, Jan. 2007.

[18] H. Hashemi, "The Indoor Radio Propagation Channel," *Proceedings of the IEEE*, vol. 81, no. 7, pp. 943-968.

[19] X. Li. and K. Pahlavan, "Super-Resolution TOA Estimation With Diversity for Indoor Geolocation," *IEEE Trans. on Wireless Communications*, vol. 3, no. 1, pp. 224-234, Jan. 2004.

[20] T.B. Vu, "Side-Lobe Control in Circular Ring Array," *IEEE Trans. on Antennas and Propagation*, vo. 41, no. 8, pp. 1143-1145, Aug. 1993.

[21] D.K. Cheng, "Optimization Techniques for Antenna Arrays," *Proceedings of the IEEE*, vol. 59, no. 12, pp. 1664-1674, Dec. 1971.

[22] N. Goto and Y. Tsunoda, "Sidelobe Reduction of Circular Arrays with a Constant Excitation Amplitude," *IEEE Trans. on Antennas and Propagation*, vol. 25, no. 6, pp. 896-898, Nov. 1977.

[23] E. Doron and M.A. Doron, "Coherent Wideband Array Processing," *IEEE Conf. on Acoustics, Speech, and Signal Processing*, pp. 497-500, March 1992.

[24] C.P. Mathews and Michael D. Zoltowski, "Performance Analysis of the UCA-ESPRIT Algorithm for Circular Ring Arrays," *IEEE Trans. on Signal Processing*, vol. 42, no. 3, Sept. 1994.

[25] A. Papoulis, "Probability, Random Variables, and Stochastic Processes, Third Edition" *McGraw-Hill, Inc.*, 1991.

[26] A. Goldsmith, "Wireless Communications," *Cambridge University Press*, pp. 78, 2005.

[27] M. Abramowitz and I.A. Stegun, "Handbook of Mathematical Functions with Formulas, Graphs, and Mathematical Tables, Ninth Edition," *Dover*, pp. 928, 1972.

[28] I. Guvenc and Z. Sahinoglu, "Threshold Selection for UWB TOA Estimation Based on Kurtosis Analysis," *IEEE Communication Letters*, vol. 9, no. 12, pp. 1025-1027, Dec. 2005.

[29] J. Fuhl, J.-P. Rossi, and E. Bonek, "High-Resolution 3-D Direction-of-Arrival Determination for Urban Mobile," *IEEE Trans. on Antennas and Propagation*, vol. 45, no. 4, pp. 672-682, April 1997.

[30] V.Y. Vu, J. Braga, X. Begaud, and B. Huyart, "Directional of arrival and time delay measurements for multi-path signals using five-port reflectometers," *IEEE Antennas and Propagation Society Symp.*, vol. 1B, pp. 735-739, 2005.

[31] T.-J. Shan, M. Wax, and T. Kailath, "On Spatial Smoothing for Direction-of-Arrival Estimation of Coherent Signals," *IEEE Trans. on Acoustics, Speech, and Signal Processing*, vol. 33, no. 4, pp. 806-811, Aug. 1985.

[32] G. Xu, R. Roy, and T. Kailath, "Detection of Number of Sources via Exploitation of Centro-Symmetry Property," *IEEE Trans. on Signal Processing*, vol. 42, no. 1, pp.102-112, Jan. 1994.

[33] P.C. Hansen and S.H. Jansen, "Prewhitening for Rank-Deficient Noise in Subspace Methods for Noise Reduction," *IEEE Trans. on Signal Processing*, vol. 53, no. 10, pp. 3718-3726, Oct. 2005.